chemosensors

MDPI

Article

Electromagnetic and Charge Transfer Enhancement Synergistically Boost the SERS Activity of Urchin-like Tungsten Oxide Nanostructures

Leilei Lan [1,2,*], Ziheng Ni [1], Yongcai Li [1], Yixue Zhang [1], Kexin Wang [1], Baichun Yao [2] and Caiye Zhao [1,*]

[1] School of Mechanics and Optoelectronic Physics, Anhui University of Science and Technology, Huainan 232001, China
[2] Tianneng Battery (Wuhu) Co., Ltd., Wuhu 241000, China
* Correspondence: leileilan@aust.edu.cn (L.L.); caiyezhao@163.com (C.Z.)

Abstract

Semiconductors are regarded as promising alternatives to traditional noble metals for constructing surface-enhanced Raman scattering (SERS) substrates. Nevertheless, their sensitivity is insufficient for widespread practical applications. In this work, urchin-like tungsten oxide (WO_3) nanostructures with different oxygen-vacancy contents are fabricated by tuning the solvothermal reaction temperature. Oxygen-vacancy-rich WO_3 nanostructures display a broad localized surface plasmon resonance band, whose resonance maximum is centered at ~585 nm. Owing to the synergistic coupling of electromagnetic enhancement and interfacial charge transfer enhancement, the as-synthesized urchin-like WO_3 nanostructures exhibit outstanding SERS sensing capability toward Rhodamine 6G molecules. The lowest detectable concentration of 1×10^{-7} M and a remarkable enhancement factor of 5.1×10^5 are achieved. The relative standard deviations below 6.5% are obtained, indicating outstanding signal uniformity of the WO_3 SERS substrates. In addition, these urchin-like WO_3 nanostructures can serve as SERS substrates for the detection of prohibited fishery drugs. This work offers a feasible strategy for fabricating high-performance semiconductor-based SERS platforms, and the plasmonic urchin-like WO_3 nanostructures show great prospects for practical chemical sensing applications.

Keywords: tungsten oxide; surface-enhanced Raman scattering sensing; localized surface plasmon resonance; charge transfer

1. Introduction

As an ultrasensitive, nondestructive, and highly efficient analytical technology, surface-enhanced Raman scattering (SERS) has attracted tremendous attention in diverse domains such as food safety, disease diagnosis, catalysis, environmental pollutant monitoring, forensics, and biomedicine [1–6]. Up to now, two primary mechanisms, including the electromagnetic mechanism and chemical mechanism, have been put forward to interpret the SERS effect [3]. In general, noble metals (Au and Ag) serve as conventional SERS-active materials, whose enhancement mechanism originates from the electromagnetic mechanism induced by the strong localized surface plasmon resonance (LSPR) effect [3]. Under laser irradiation, LSPR can generate greatly amplified local electromagnetic fields near the surface of nanostructured noble metals, which dominates the SERS signal amplification process. Noble metal substrates deliver ultrahigh detection sensitivity, and single-molecule detection can even be realized under optimal experimental conditions [7,8]. For example, Chen et al.

Check for updates

Received: 23 August 2026
Revised: 22 October 2026
Accepted: 26 October 2026
Published: 29 October 2026

Copyright: © 2026 by the authors. Licensee MDPI, Basel, Switzerland. This article is an open access article distributed under the terms and conditions of the Creative Commons Attribution (CC BY) license.

designed gold and silver nanohole arrays integrated within a metal-insulator-metal configuration and further decorated with silver nanoparticles, yielding substrates with excellent SERS performance [9]. However, noble metal substrates suffer from inherent drawbacks including high production expenses, strong spectral noise, and low experimental reproducibility [10]. In recent years, a variety of semiconductor materials, including graphene, transition metal chalcogenides, transition metal oxides, and covalent-organic frameworks, have been demonstrated to exhibit attractive SERS activity, offering new opportunities for developing noble-metal-free SERS sensing platforms [11–18]. For example, Tang and coworkers demonstrated that the band structure of transition metal chalcogenides can be precisely tuned via alloy engineering, which further achieves the on-demand controllable preparation of high-performance SERS substrates [16]. Fan and coworkers reported an innovative sensing strategy that combines the enhanced light-matter interactions of a single ZnO whispering-gallery-mode cavity with the fingerprint spectral feature of SERS to achieve ultrasensitive and highly specific molecular detection [17]. Ge et al. developed an optimized electrochemical cathodic exfoliation method to fabricate high-yield, low-defect MSe_2 (M = Ta, Nb, Ti) monolayers, whose excellent SERS sensitivity enables superior tear-fluid MMP-9 detection performance [18]. For semiconductor-based SERS substrates, chemical enhancement constitutes the major enhancement contribution, which arises from the interfacial charge transfer process occurring between semiconductor substrates and analyte molecules. Benefiting from their intrinsic material characteristics, semiconductor-based SERS substrates exhibit superior stability, good signal uniformity, and abundant sources [11]. Nevertheless, compared with conventional noble metals, semiconductor-based SERS substrates suffer from relatively weak signal amplification. The unsatisfactory sensitivity has become a critical bottleneck that restricts their wide practical applications.

Benefiting from precise electronic structure modulation strategies including oxygen vacancy engineering, doping, and phase transformation, plasmonic semiconductors fundamentally overcome the intrinsic limitation of conventional semiconductor-based SERS substrates, which solely depend on weak interfacial charge transfer to produce chemical enhancement. Instead, such materials integrate LSPR-derived electromagnetic field amplification with interfacial charge transfer induced chemical enhancement, constructing a dual synergistic enhancement system that greatly improves their SERS sensitivity [19–21]. For example, Li et al. demonstrated that reducing semiconducting TiO_2 microspheres into quasi-metallic Ti_3O_5 microspheres boosted SERS sensitivity by 10,000 times [19]. Meng and coworkers designed amorphous MoO_3 monolayers with visible-region LSPR activity for trace detection of carcinogenic aromatic amines, achieving a low limit of detection of 10^{-9} M for o-aminoazotoluene [20]. However, precisely tailoring the LSPR peak position to achieve spectral matching with the excitation laser still remains challenging.

Herein, we report that urchin-like tungsten oxide (WO_3) nanostructures synthesized via a solvothermal approach can serve as high-sensitivity SERS substrates. By adjusting the reaction temperature, oxygen-vacancy-rich urchin-like WO_3 nanostructures show an LSPR band ranging from 400 to 770 nm, with its resonance maximum centered at ~585 nm. Benefiting from the synergistic coupling of electromagnetic enhancement and interfacial charge transfer enhancement, the as-synthesized urchin-like WO_3 nanostructures display excellent SERS sensing performance, achieving a lowest detectable concentration of 1×10^{-7} M and an enhancement factor (EF) of 5.1×10^5 for Rhodamine 6G (R6G) molecules. In addition, prohibited fishery drugs can be detected by using urchin-like WO_3 nanostructures as SERS substrates. The present work provides a viable approach to design high-performance semiconductor-based SERS platforms, and the plasmonic urchin-like WO_3 nanostructures hold enormous potential for practical chemical sensing applications.

https://doi.org/10.3390/chemosensors14110245

2. Materials and Methods

2.1. Preparation of Urchin-like WO_3 Nanostructures

In a typical synthetic procedure, 35 mg of tungsten hexachloride (WCl_6, Aladdin Reagent Co., Ltd., Shanghai, China) powder was uniformly dispersed in 30 mL of absolute ethanol (Aladdin Reagent Co., Ltd., Shanghai, China) under continuous magnetic stirring. Subsequently, the well-mixed solution was transferred into a 50 mL Teflon-lined autoclave (KZ50, Beijing Zhouyun Technology Co., Ltd., Beijing, China). The autoclave was tightly sealed and heated to 160–190 °C for 24 h. After natural cooling to ambient temperature, the precipitated products were collected and thoroughly rinsed with deionized water (Genie G, RephiLe Bioscience, Ltd., Shanghai, China) and absolute ethanol in sequence to remove residual impurities and unreacted precursors. The washing process was repeated via centrifugation (GT216C, Hunan Kecheng Instrument Equipment Co., Ltd., Changsha, China) for three cycles to achieve high-purity samples. Ultimately, the obtained solid powders were dried in a vacuum oven (DZF6050, Shaoxing Supo Instrument Co., Ltd., Shaoxing, China) at 60 °C for 8 h to remove residual solvent, yielding the final urchin-like WO_3 nanostructures.

2.2. Characterization

X-ray diffraction (XRD) patterns were collected on an X-ray diffractometer (Rigaku Smartlab (3), Akishima, Tokyo, Japan). The microscopic morphology and internal nanostructure were investigated by transmission electron microscopy (TEM, FEI Tecnai G2 T20, Hillsboro, OR, USA) and scanning electron microscopy (SEM, FEI XL-30, Eindhoven, The Netherlands). X-ray photoelectron spectroscopy (XPS) measurements were performed on a Thermofisher ESCALAB 250Xi apparatus (Waltham, MA, USA). Ultraviolet-visible (UV-vis) absorption spectra were recorded to explore the optical absorption behaviour and LSPR properties of the samples (Shimadzu UV-3600, Kyoto, Japan).

2.3. Raman Measurement

To investigate the SERS performance of urchin-like WO_3 nanostructures, R6G (Shanghai Macklin Biochemical Co., Ltd., Shanghai, China) dissolved in deionized water was selected as the probe molecule. A stock R6G solution (1×10^{-3} M) was first prepared. A series of working solutions spanning from 1×10^{-4} M to 1×10^{-7} M were subsequently obtained by diluting the stock solution. Preparation of the WO_3 samples for SERS measurements: 5 mg of WO_3 powder was added to 5 mL of R6G solution with different concentrations. The mixture was stirred for 2 h, and the precipitate was collected by centrifugation. Afterwards, a small amount of R6G-modified WO_3 powder was placed on a glass slide and dried at room temperature in the dark for 4 h. To improve the signal uniformity, a glass slide was used to gently press the powder into a flat layer prior to SERS measurement. The excitation wavelength was 532 nm and a 50× objective was used to focus the laser beam (LabRAM HR, HORIBA Jobin Yvon S.A.S., Longjumeau, France). The spectra were acquired for 10 s and the laser power was maintained at 0.25 mW with an average spot diameter of 1.0 μm in all acquisitions. The silicon peak at 520 cm^{-1} was used to calibrate the measured wavenumbers. A silicon substrate was employed for non-SERS reference measurements.

3. Results and Discussion

3.1. Characterization of Urchin-like WO_3 Nanostructures

XRD patterns of the as-synthesized urchin-like WO_3 nanostructures (marked WO_3-160, WO_3-175, and WO_3-190) with different reaction temperatures (160 °C, 175 °C, and 190 °C) are shown in Figure 1a. Several diffraction peaks at 23.4, 24.1, 26.5, 28.6, 34.0, 41.5, 47.7,

49.7, and 55.7° can be clearly observed, which are assignable to the (001), (200), (102), (112), (220), (222), (002), (400), and (420) planes of the orthorhombic WO_3 (JCPDS No. 20-1324, a = 0.7384 nm, b = 0.7512 nm, c = 0.3846 nm), respectively [22]. Further structural characterization was performed by Raman spectroscopy in the range from 400 to 1200 cm^{-1}. Two characteristic vibration peaks can be detected at 689 and 804 cm^{-1} (Figure 1b). The peak at 689 cm^{-1} is assigned to the stretching vibration of W-O bond, while the other peak at 804 cm^{-1} is assigned to the stretching vibration of O-W-O bond [23]. The results indicate that WO_3 samples are successfully synthesized by the solvothermal method.

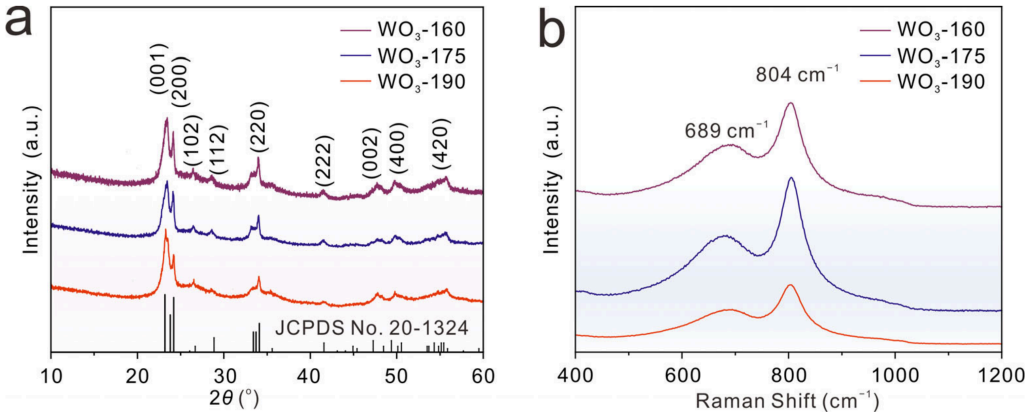


Figure 1. (**a**) XRD patterns and (**b**) Raman spectra of as-prepared urchin-like WO_3 nanostructures.

XPS measurements were carried out to further investigate the surface chemical state of WO_3. The XPS survey spectra of WO_3-160, WO_3-175, and WO_3-190 clearly display the characteristic photoemission peaks assigned to W, O, and C elements (Figure S1). As shown in Figure 2a–c, high-resolution W 4f spectra can be deconvoluted into two spin–orbit doublets. A Shirley-type background is subtracted from the acquired spectrum prior to curve-fitting analysis. The spin–orbit doublet separation is maintained at 2.1 ± 0.1 eV for the W states [24]. The doublet centred at 34.4 and 36.6 eV corresponds to the W $4f_{7/2}$ and W $4f_{5/2}$ core-level signals of W^{5+}, whereas the second doublet at 35.7 and 37.9 eV originates from the W $4f_{7/2}$ and W $4f_{5/2}$ core-level signals of W^{6+} [25]. On the basis of the deconvolution results, the atomic fractions of W^{5+} and W^{6+} in WO_3-190 are 19.3% and 80.7%, respectively. By contrast, the proportion of W^{5+} rises to 41.2% while that of W^{6+} drops to 58.8% for WO_3-160. All fitting results are summarized in Table S1. The increased proportion of W^{5+} is mainly associated with the formation of positively charged oxygen vacancies and the concomitant presence of charge-compensating electrons [26,27]. The oxygen vacancy was also confirmed by the XPS O 1s spectra. As shown in Figure 2d–f, the spectra can be deconvoluted into three peaks. The peaks at 530.6 and 532.7 eV can be assigned to the W-O-W lattice oxygen (O_L) bonds of WO_3 and surface-adsorbed oxygen (O_A), respectively [28]. The peak at 531.5 eV is attributed to oxygen species chemisorbed on oxygen vacancies (O_V) [29]. Compared with WO_3-190 and WO_3-175, WO_3-160 exhibits a higher relative area fraction of the peak at 531.5 eV, demonstrating the presence of more oxygen vacancies in WO_3-160. The fractions of the oxygen-vacancy-related O 1s component are 34.2%, 28.1%, and 24.6% for WO_3-160, WO_3-175, and WO_3-190, respectively (Table S1). XPS measurements demonstrate that the concentration of oxygen vacancies can be effectively tuned by modifying the reaction temperature, and similar observations have also been reported in previous studies [30].

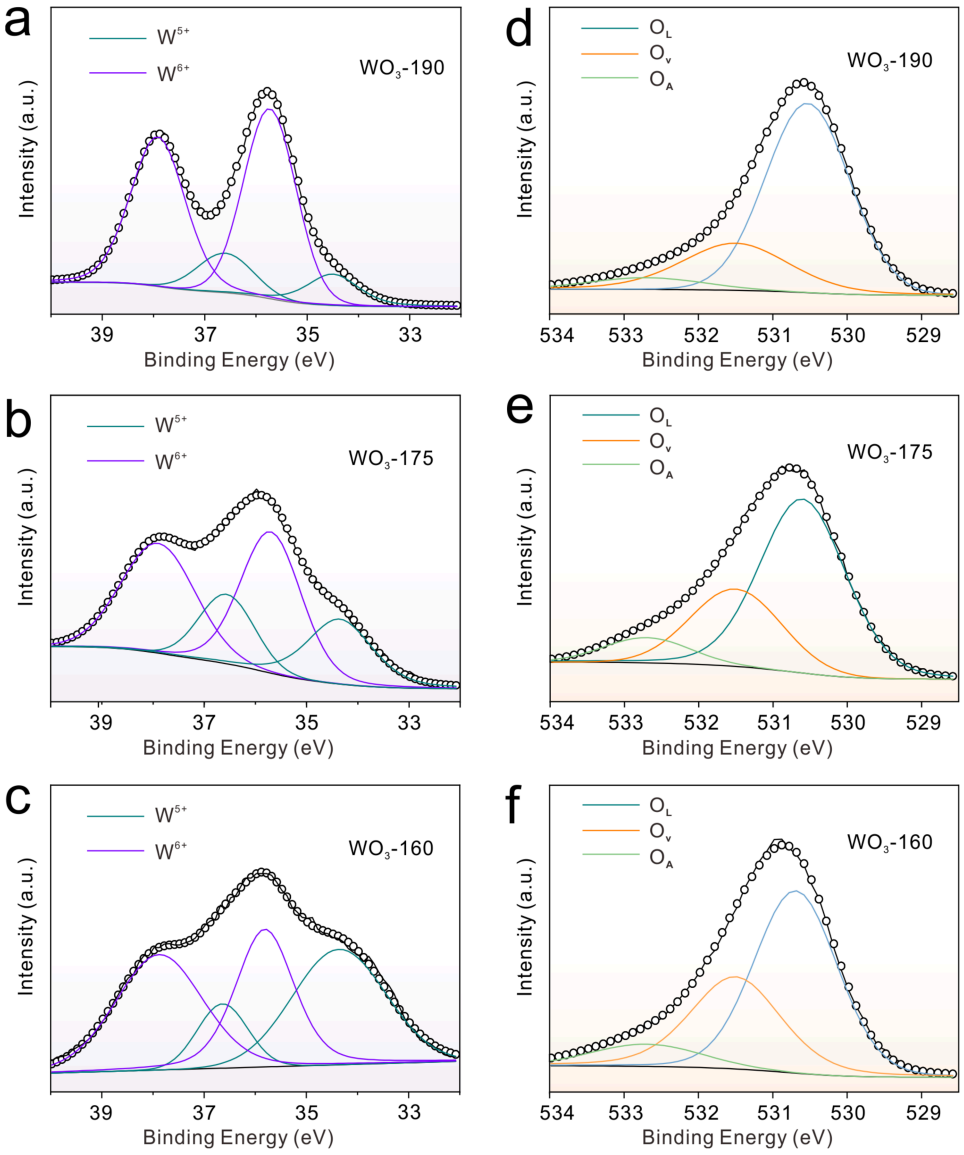


Figure 2. XPS W 4f spectra of (**a**) WO_3-190, (**b**) WO_3-175, and (**c**) WO_3-160 nanostructures. XPS O 1s spectra of (**d**) WO_3-190, (**e**) WO_3-175, and (**f**) WO_3-160 nanostructures.

SEM and TEM techniques were utilized to observe the surface morphology and microscopic structure of the as-prepared WO_3 nanostructures. As illustrated in Figure 3a–f, as-prepared WO_3-160, WO_3-175, and WO_3-190 nanostructures have a typical urchin-like shape, with an average diameter ranging from 1 to 3 μm. The elemental mapping results of WO_3-160 demonstrate the uniform distribution of W and O elements across the as-prepared nanostructures (Figure 3g,h), indicating the homogeneous composition of the obtained samples. Further SEM observation in Figure S2 reveals that these urchin-like WO_3 nanostructures feature a distinct hollow interior cavity. As shown in Figure 3i, the radially grown nanoneedle subunits of the urchin-like architecture possess a length of 100-400 nm. The results verify the successful fabrication of urchin-like WO_3 nanostructures. The formation mechanism of urchin-like WO_3 nanostructures involves nucleation, anisotropic growth, and Ostwald self-assembly processes [31,32]. First, the tungsten precursor reacts to form numerous primary WO_3 nuclei. Benefiting from the intrinsic anisotropic crystal property of WO_3, crystal growth preferentially proceeds along a specific crystallographic direction. One-dimensional nanoneedles radially extend from the surface of spherical aggregates. With prolonged solvothermal reaction, smaller grains dissolve and redeposit on larger

crystals via Ostwald ripening. The nanoneedles continuously grow, finally constructing the urchin-like hierarchical architecture assembled from radially aligned nanoneedles. These radially distributed nanoneedles create abundant 'hotspots' (Figure S3), which can contribute to electromagnetic enhancement. In addition, the urchin-like morphology possesses a large specific surface area, offering sufficient adsorption sites for probe molecules and increasing the loading amount of probe molecules. Therefore, the urchin-like morphology endows the WO_3 substrate with favorable features for SERS performance.

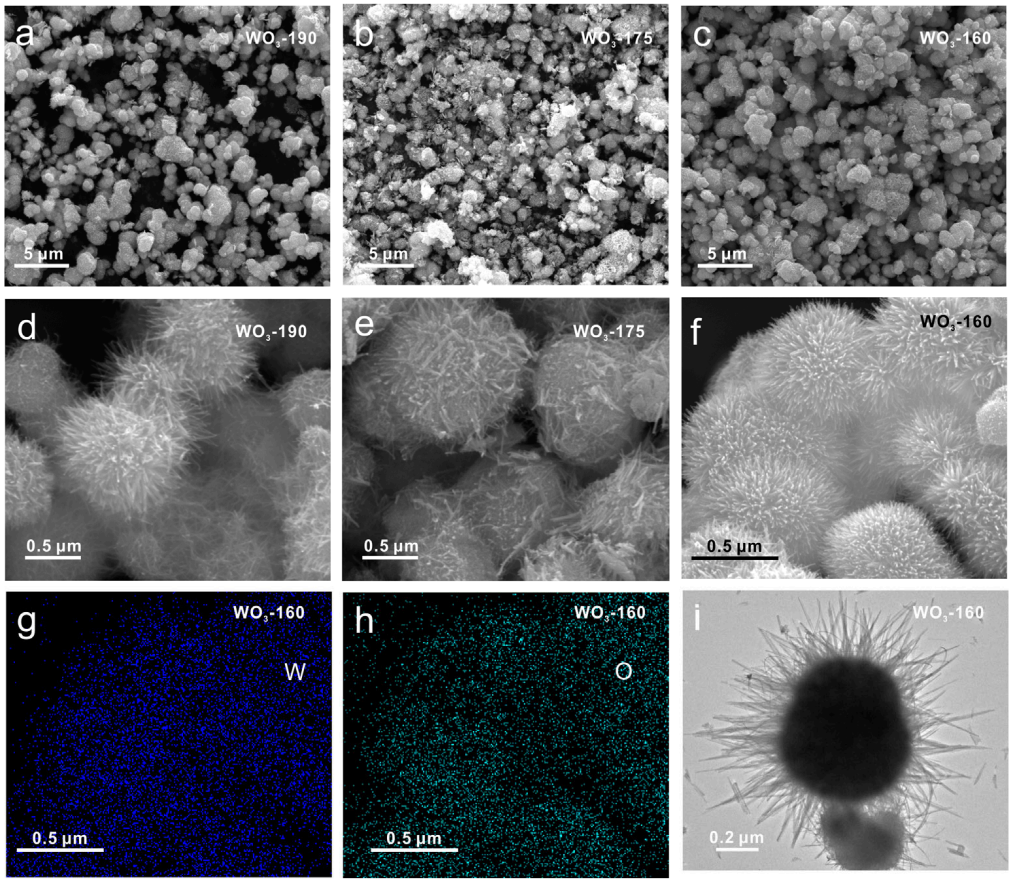


Figure 3. (**a**–**f**) SEM images, (**g**,**h**) elemental mapping images from (**f**), and (**i**) TEM image of the as-prepared urchin-like WO_3 nanostructures.

3.2. SERS Performances of Urchin-like WO_3 Nanostructures

R6G molecule was used to examine the SERS performance of urchin-like WO_3 nanostructures. SERS spectra of 1×10^{-5} M R6G adsorbed on urchin-like WO_3-160, WO_3-175, and WO_3-190 nanostructures are displayed in Figure 4a. Several typical characteristic peaks of R6G at P_1 (612 cm^{-1}), P_2 (774 cm^{-1}), and P_3 (1360 cm^{-1}) can be distinctly detected. Specifically, the peaks at 612 and 774 cm^{-1} originate from the C-C-C ring in-plane bend and C-H out-of-plane bend modes, respectively. The peak at 1360 cm^{-1} is attributed to the aromatic C-C stretching mode [33]. The results indicate that as-prepared WO_3 samples can be used as SERS-active materials. Compared with WO_3-175 and WO_3-190, the WO_3-160 exhibits stronger SERS enhancement. The enhanced Raman intensities of R6G at 612 cm^{-1} on WO_3-160 are ~1.5 times higher than those on WO_3-190 (Figure 4b).

On this basis, SERS signals of R6G at various concentrations were further acquired on WO_3-160 substrates. It is worth noting that distinct SERS fingerprints of R6G are still

observable at a trace concentration of 1×10^{-7} M (Figure 5a). The Raman EF can be calculated using the equation presented below [34]:

$$EF = \frac{I_{SERS}}{I_{Raman}} \times \frac{N_{Raman}}{N_{SERS}} \quad (1)$$

where I_{SERS} and I_{Raman} represent the peak intensities obtained from SERS and conventional Raman spectra, respectively. N_{SERS} and N_{Raman} refer to the average number of analyte molecules within the laser scattering region during SERS and conventional Raman measurements, respectively. The Raman EF of WO_3-160 was calculated to be 5.1×10^5 (detailed calculation processes are provided in the Supplementary Materials), exhibiting comparable SERS capacity to conventional noble metal materials without 'hotspots'. Figure 5b presents the working curve plotting logarithmic-scale Raman intensity against R6G concentration. A well-defined linear relationship is achieved over the concentration range from 1×10^{-4} M to 1×10^{-7} M, with a correlation coefficient (R^2) of 0.976. This result demonstrates that WO_3-160 nanostructures possess potential for SERS quantitative analysis. In addition, the SERS signal intensities of samples from two tested batches are comparable (Figure S5), indicating consistent performance of as-prepared WO_3-160 substrates.

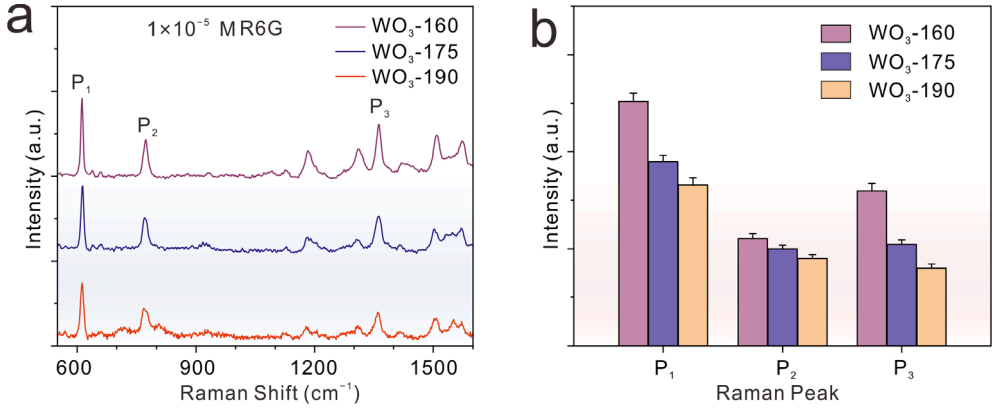


Figure 4. (**a**,**b**) SERS spectra and corresponding signal intensity of R6G (1×10^{-5}) adsorbed on the as-prepared urchin-like WO_3-160 and WO_3-175, WO_3-190 nanostructures.

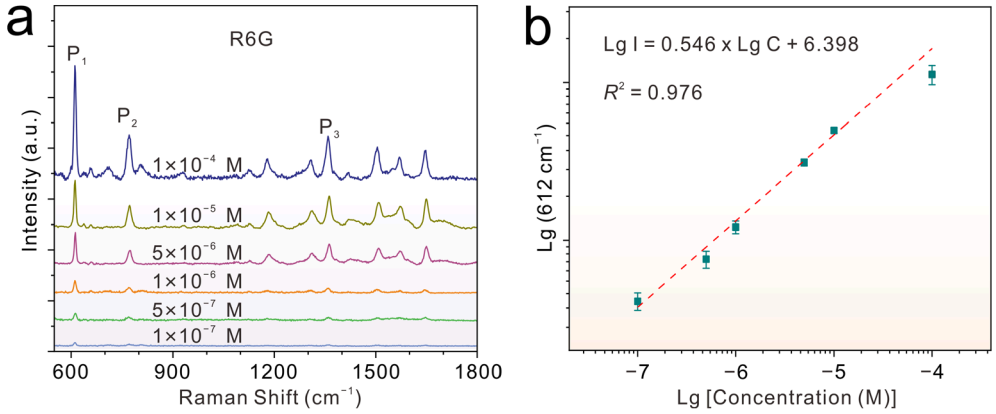


Figure 5. (**a**) SERS spectra of R6G with a series of concentrations adsorbed on the as-prepared urchin-like WO_3-160 nanostructures. (**b**) Logarithm of integral Raman intensity at 612 cm^{-1} as a function of molecular concentration, and corresponding fitting curves.

SERS spectra of 1×10^{-5} M R6G adsorbed on the urchin-like WO_3-160 nanostructures at 30 randomly selected points (spot-to-spot distance is about 2 μm) were collected (Figure 6a). The RSDs of Raman intensities at 612 and 774 cm^{-1} of R6G molecules on urchin-like WO_3-160 nanostructures are calculated to be 5.5% and 6.3%, respectively (Figure 6b,c), which

are generally lower than those of traditional Au and Ag SERS materials [35–37], indicating good SERS signal uniformity of urchin-like WO_3-160 substrates.

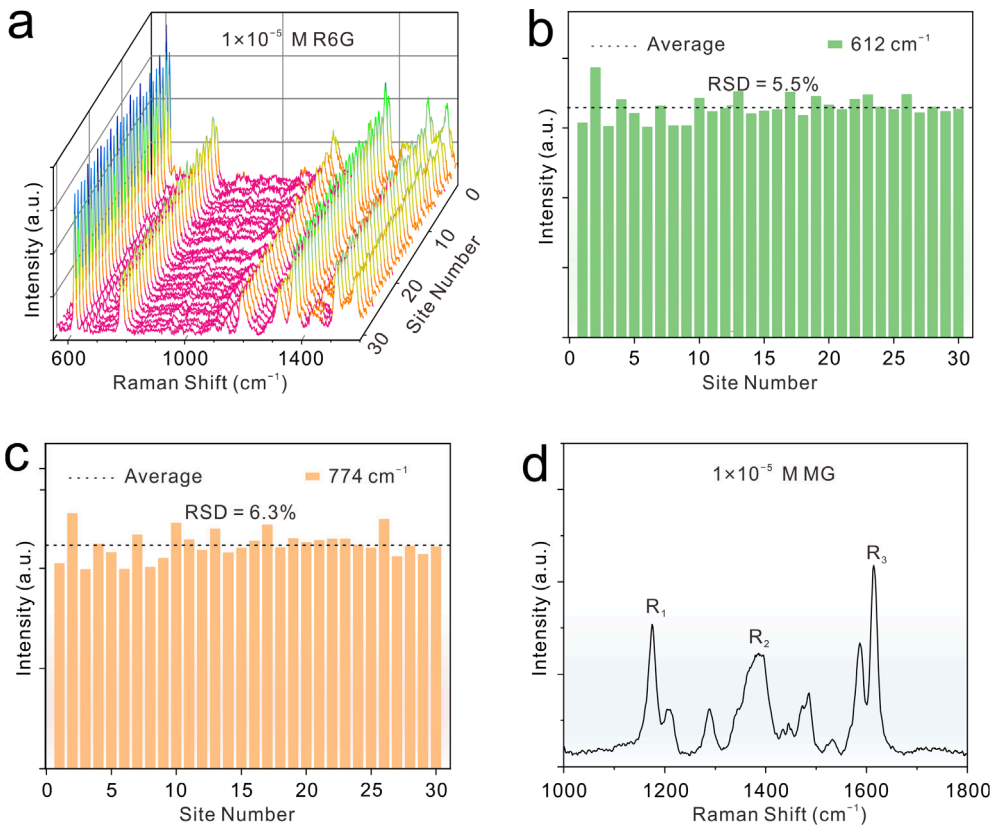


Figure 6. (**a**) SERS spectra of 1 × 10^{-5} M R6G adsorbed on the as-prepared urchin-like WO_3-160 nanostructures at 30 randomly selected points. (**b**,**c**) The RSDs of Raman intensities at 612 and 774 cm^{-1} of R6G molecules acquired from (**a**). (**d**) SERS spectrum of 1 × 10^{-5} M MG adsorbed on the as-prepared urchin-like WO_3-160 nanostructures.

In addition, malachite green (MG) is a prohibited fishery drug, which can be detected by using WO_3-160 as a SERS substrate. As shown in Figure 6d, main characteristic Raman peaks of MG at 1175 (R_1, in-plane mode of C-H bending), 1385 (R_2, N-phenyl stretching), and 1614 cm^{-1} (R_3, C-C stretching) are observed [38], indicating that WO_3-160 has promising applications for food safety monitoring.

3.3. Raman Enhancement Mechanism of Urchin-like WO_3 Nanostructures

To explore the underlying Raman enhancement mechanism, UV-vis absorption spectral characterizations were performed. Compared with WO_3-175 and WO_3-190, WO_3-160 exhibits a distinct LSPR band ranging from 400 to 770 nm, with the maximum resonance at ~585 nm (Figure 7a). According to the Drude model, the plasma frequency of metal oxides is strongly dependent on their free-electron density, which is primarily determined by the concentration of oxygen vacancies [39]. Higher oxygen-vacancy concentration gives rise to greater free-electron density, which gradually blue-shifts the LSPR peak of metal oxides from the near-infrared into the visible range. Therefore, the characteristic plasmonic resonance peak observed for WO_3-160 originates from its high density of oxygen-vacancy defects (Table S1). The LSPR effect can amplify the local electric field on the surface of materials, and the amplification of Raman signals arising from electromagnetic enhancement is approximately proportional to the fourth power of the enhancement of the local electric field. Since the 532 nm excitation laser line falls within this resonance region, efficient electromag-

netic enhancement is achieved for SERS detection in the R6G-WO_3-160 system. The optical band gap of the WO_3 nanostructures can be obtained from the absorption-edge data based on the Tauc relation $\alpha hv = A(hv - E_g)^2$, where α, h, v, E_g and A represent the absorption coefficient, Planck's constant, light frequency, band gap, and a constant, respectively [40]. From the $(\alpha hv)^{1/2}$ versus energy (hv) plot presented in Figure 7b, the band gaps of the WO_3-190, WO_3-175 and WO_3-160 are estimated to be 2.57, 2.53, and 2.50 eV, respectively. Further, the degree of charge transfer ($\rho_{CT}(k)$) is used to evaluate the contribution of charge transfer effect to SERS intensity, as expressed by the following equation [41]:

$$\rho_{CT}(k) = \frac{I^k(CT) - I^k(SPR)}{I^k(CT) + I^0(SPR)} \quad (2)$$

where $I^k(CT)$ represents the Raman intensity of a vibrational mode whose enhancement originates from the charge transfer. Two reference intensities without charge transfer contribution are chosen within a spectral region. Among them, $I^0(SPR)$ denotes the intensity of the totally symmetric mode enhanced solely by surface plasmon resonance (SPR). The other is called $I^k(SPR)$. If the k band is a totally symmetric vibration band, the main contribution to the intensity arises from the SPR, and $I^k(SPR) = I^0(SPR)$. For a nontotally symmetric vibrational band k, charge-transfer effects dominate the SERS enhancement. At this moment, $I^k(SPR)$ is typically very weak and can be reasonably set to zero for most calculations. We selected the totally symmetric 1360 cm^{-1} mode and the nontotally symmetric 612 cm^{-1} mode of R6G molecules as the 0 and k bands, respectively. The degrees of charge transfer calculated for R6G (1×10^{-5} M) on WO_3-190, WO_3-175, and the WO_3-160 are 0.674, 0.644, and 0.612, respectively. This result indicates that WO_3-160 exhibits a more prominent electromagnetic enhancement effect, which boosts the overall SERS performance.

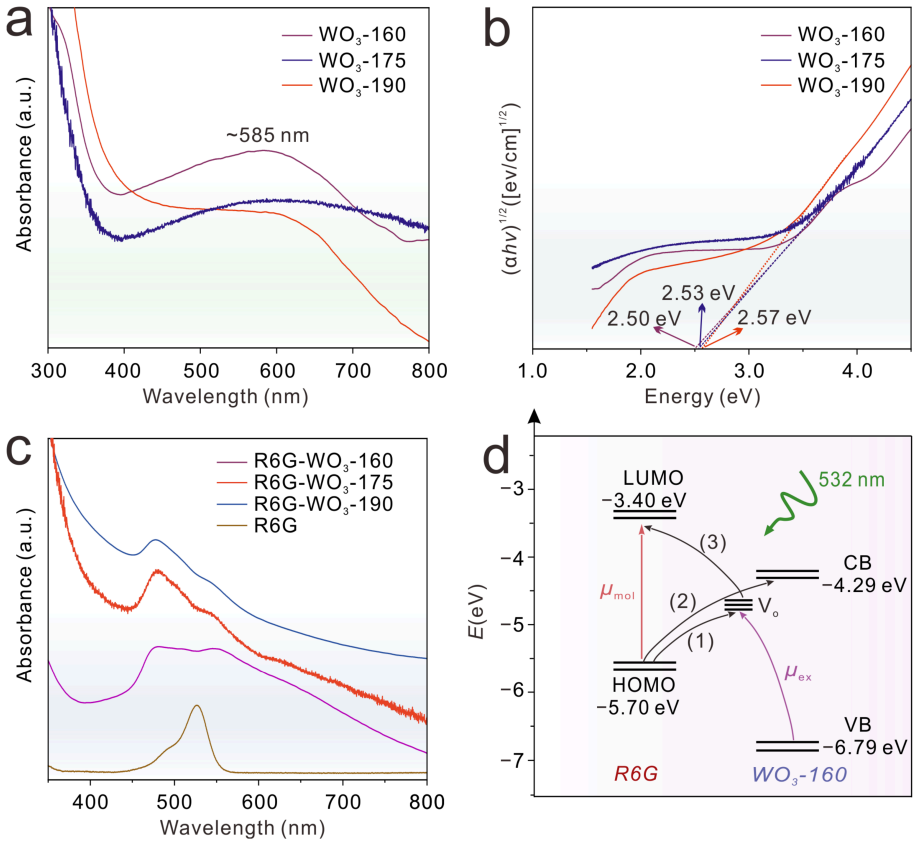


Figure 7. (**a**) UV-vis absorption spectra of WO_3-160, WO_3-175, and WO_3-190. (**b**) Optical band gaps of WO_3-160, WO_3-175, and WO_3-190. (**c**) UV-vis absorption spectra of R6G molecule, R6G-WO_3-160, R6G-WO_3-175, and R6G-WO_3-190. (**d**) The energy level diagram of R6G adsorbed on WO_3-160.

In Figure 7c, R6G shows an intense characteristic absorption band centered at ~528 nm. Compared with the spectra of R6G and WO_3-160, the spectrum for the R6G-WO_3-160 displays two new bands at ~480 and ~545 nm, which may be attributed to interfacial charge transfer processes between WO_3-160 and adsorbed R6G [42,43]. Similar phenomena are also observed for R6G-WO_3-175 and R6G-WO_3-190. Figure S6 presents the Raman spectra of R6G adsorbed on bare Si and WO_3-160 without baseline correction. A strong fluorescence background appears on bare Si and the Raman signals of R6G cannot be observed. Nevertheless, such fluorescence background is greatly suppressed when R6G molecules are adsorbed on WO_3-160. This notable quenching behavior may be indicative of efficient charge transfer processes at the R6G-WO_3-160 interface [44]. The energy level diagram of R6G adsorbed on WO_3-160 is illustrated in Figure 7d. The conduction band (CB) and valence band (VB) positions of WO_3-160 are evaluated via the relationships $E_{CB} = -X + E_g/2$ and $E_{VB} = -X - E_g/2$, respectively [40]. Herein, X denotes the absolute electronegativity of the atom semiconductor, defined as the geometric mean of the absolute electronegativity of the constituent atoms. E_g corresponds to the experimental band gap of the WO_3-160 (2.50 eV, from Figure 7b). The calculated absolute electronegativity X for WO_3-160 is 5.54 eV. According to the above equations, the CB and VB positions of WO_3-160 are calculated to be −4.29 and −6.79 eV, respectively. The defect energy levels originating from oxygen vacancies are well separated from the bottom of the CB and located at 0.5–1.0 eV below the CB edge [25]. Furthermore, the energy levels of R6G molecule reveal that its highest occupied molecular orbital (HOMO) and lowest unoccupied molecular orbital (LUMO) are located at −5.70 and −3.40 eV, respectively [40]. Based on the thermodynamic feasibility in this system, the following photo-induced charge transfer (PICT) pathways can be identified: PICT between molecular HOMO level and oxygen vacancy-associated electronic states, PICT between molecular HOMO level and CB state, and PICT between oxygen vacancy-associated electronic states and molecular LUMO level. According to Herzberg-Teller coupling theory, $R_{\text{mol-CT}}(\omega)$ and $R_{\text{ex-CT}}(\omega)$ can be described as [10]:

$$R_{\text{mol}-\text{CT}}(\omega) = \frac{\mu_{\text{mol}}\mu_{\text{CT}}h_{\text{mol}-\text{CT}}\langle i|Q_k|f\rangle}{\left((\varepsilon_1(\omega)+2\varepsilon_0)^2+\varepsilon_2^2\right)\left((\omega_{\text{CT}}^2-\omega^2)+\gamma_{\text{CT}}^2\right)\left((\omega_{\text{mol}}^2-\omega^2)+\gamma_{\text{mol}}^2\right)} \quad (3)$$

$$R_{\text{ex}-\text{CT}}(\omega) = \frac{\mu_{\text{ex}}\mu_{\text{CT}}h_{\text{ex}-\text{CT}}\langle i|Q_k|f\rangle}{\left((\varepsilon_1(\omega)+2\varepsilon_0)^2+\varepsilon_2^2\right)\left((\omega_{\text{CT}}^2-\omega^2)+\gamma_{\text{CT}}^2\right)\left((\omega_{\text{ex}}^2-\omega^2)+\gamma_{\text{ex}}^2\right)} \quad (4)$$

where ω represents the frequency of the incident photons, ω_{mol} is the molecular resonance frequency, and ω_{ex} is the exciton resonance frequency. The Raman intensity is proportional to the values of ${R^2}_{\text{mol-CT}}(\omega)$ and ${R^2}_{\text{ex-CT}}(\omega)$. Under irradiation with a 532 nm laser, the corresponding excitation energy is 2.33 eV. The intrinsic band gap of R6G molecule is determined to be 2.30 eV according to the difference between LUMO and HOMO energy levels. Since the photon energy of 532 nm laser closely matches the band gap of R6G ($\omega \approx \omega_{\text{mol}}$), the molecular transition (μ_{mol}) can be effectively excited. Furthermore, electron transition energy between oxygen vacancy-associated electronic states and VB state is 2.0 eV ($\omega \approx \omega_{\text{ex}}$), which gives rise to exciton resonance (μ_{ex}). The molecular resonance and exciton resonance greatly facilitate the interfacial charge transfer between WO_3 and adsorbed R6G molecules, which contributes to the enhancement of molecular Raman signals [45]. Accordingly, the SERS activity of the urchin-like WO_3-160 nanostructures stems from the synergistic coupling of electromagnetic enhancement and interfacial charge transfer enhancement.

4. Conclusions

In summary, urchin-like WO_3 nanostructures are successfully synthesized via a facile solvothermal approach. By adjusting the reaction temperature, the LSPR band of oxygen-

vacancy-rich WO_3 nanostructures possesses a broad region from 400 to 770 nm, with the maximum peak at ~585 nm. These urchin-like WO_3 nanostructures exhibit remarkable SERS performance for R6G, achieving a high Raman EF of 5.1×10^5 and the lowest detectable concentration of 1×10^{-7} M. The RSDs lower than 6.5% are achieved, indicating excellent signal uniformity of urchin-like WO_3 nanostructures. In addition, prohibited fishery drugs can be detected by using urchin-like WO_3 nanostructures as SERS substrates. The remarkable SERS activity of urchin-like WO_3 nanostructures originates from the synergistic coupling of electromagnetic enhancement and interfacial charge transfer enhancement. This work provides a viable strategy to construct high-performance semiconductor-based SERS substrates, and the plasmonic urchin-like WO_3 nanostructures possess considerable potential for practical sensing applications.

Supplementary Materials: The following supporting information can be downloaded at https://www.mdpi.com/article/10.3390/chemosensors14110245/s1, Figure S1: XPS survey spectra of WO_3-160, WO_3-175, and WO_3-190 nanostructures; Figure S2: SEM image of the urchin-like WO_3-160 nanostructures; Figure S3: TEM image of the urchin-like WO_3-160 nanostructures; Figure S4: The Raman spectrum of bulk R6G with 10 s acquisition time; Figure S5: Raman spectra of R6G (1×10^{-5} M) adsorbed on WO_3-160 with different batchs; Figure S6: Raman spectra of R6G (1×10^{-6} M) adsorbed on bare Si and WO_3-160 without baseline correction; Table S1: Atomic percentages of W^{6+}, W^{5+} and O_V on the as-prepared WO_3-160, WO_3-175 and WO_3-190 nanostructures.

Author Contributions: Conceptualization, L.L., Y.Z. and K.W.; data curation, L.L., Y.L. and K.W.; formal analysis, Z.N., Y.L. and C.Z.; funding acquisition, L.L. and C.Z.; investigation, Z.N., Y.Z., K.W. and B.Y.; methodology, Z.N., Y.L. and K.W.; project administration, L.L., K.W. and B.Y.; resources, B.Y. and C.Z.; supervision, K.W., B.Y. and C.Z.; validation, Z.N., Y.L., Y.Z. and B.Y.; visualization, L.L., Z.N. and Y.Z.; writing—original draft, L.L. and Z.N.; writing—review and editing, Y.Z., B.Y. and C.Z. All authors have read and agreed to the published version of the manuscript.

Funding: This research was funded by the Scientific Research Foundation for High-level Talents of Anhui University of Science and Technology (grant number 2022yjrc91) and Anhui Postdoctoral Scientific Research Program Foundation (grant number 2026C1481).

Institutional Review Board Statement: Not applicable.

Informed Consent Statement: Not applicable.

Data Availability Statement: The original contributions presented in this study are included in the article. Further inquiries can be directed to the corresponding author.

Acknowledgments: We gratefully acknowledge the assistance and instruction from Yangjin Zhang of the Shiyanjia Lab for XPS measurements. During the preparation of this manuscript/study, the authors used Doubao (generative-AI tool) for the purposes of English-language polishing. The authors have reviewed and edited the output and take full responsibility for the content of this publication.

Conflicts of Interest: Author Baichun Yao was employed by the company Tianneng Battery (Wuhu) Co., Ltd. The remaining authors declare that the research was conducted in the absence of any commercial or financial relationships that could be construed as a potential conflict of interest.

References

1. Lovasz, V.D.; Gonçalves, J.M.; Vinnacombe-Willson, G.A.; Liz-Marzán, L.M.; Villa, K. Nanoengineered photoactive micromotors for targeted pollutant capture, degradation, and SERS-based detection. *Research* **2026**, *9*, 1110. [CrossRef] [PubMed]
2. Sim, S.B.; Haizan, I.; Choi, M.Y.; Lee, Y.; Choi, J.H. Recent strategies for microRNA detection: A comprehensive review of SERS-based nanobiosensors. *Chemosensors* **2024**, *12*, 154. [CrossRef]
3. Jiang, L.; Hassan, M.M.; Ali, S.; Li, H.H.; Sheng, R.; Chen, Q.S. Evolving trends in SERS-based techniques for food quality and safety: A review. *Trends Food Sci. Technol.* **2021**, *112*, 225–240. [CrossRef]

4. Langer, J.; Jimenez de Aberasturi, D.; Aizpurua, J.; Alvarez-Puebla, R.A.; Auguie, B.; Baumberg, J.J.; Bazan, G.C.; Bell, S.E.J.; Boisen, A.; Brolo, A.G.; et al. Present and future of surface-enhanced Raman scattering. *ACS Nano* **2020**, *14*, 18–117. [CrossRef] [PubMed]
5. Trinh, B.T.; Nguyen, S.K.; Kim, D.; Nguyen, H.Q.; Lee, J.; Sohn, Y.; Yoon, I. Cellulose-based SERS substrate for vapor-phase thiol detection with PCA for enhanced chemical selectivity. *Chemosensors* **2025**, *13*, 101. [CrossRef]
6. Zhang, M.J.; Liu, A.C.; Zhang, J.Y.; Meng, X.Y.; Wang, Y.N.; Song, X.Y.; Xie, Y.J.; Xu, L.; Lin, J.; Wang, X.T.; et al. Chemical engineering of heterojunction SERS substrates: Emerging tools for disease diagnosis and health monitoring. *SmartMat* **2025**, *6*, e70045. [CrossRef]
7. Wang, T.J.; Chang, H.W.; Chen, J.S.; Chiang, H.P. Nanotip-assisted photoreduction of silver nanostructures on chemically patterned ferroelectric crystals for surface enhanced Raman scattering. *Sci. Rep.* **2019**, *9*, 10962. [CrossRef] [PubMed]
8. Lai, C.H.; Wang, G.A.; Ling, T.K.; Wang, T.J.; Chiu, P.K.; Chau, Y.F.C.; Huang, C.C.; Chiang, H.P. Near infrared surface-enhanced Raman scattering based on star-shaped gold/silver nanoparticles and hyperbolic metamaterial. *Sci. Rep.* **2017**, *7*, 5446. [CrossRef] [PubMed]
9. Chen, S.H.; Wang, Y.C.; He, X.R.; Liang, H.C.; Chiang, H.P. Plasmon-enhanced photoluminescence and SERS in Ag- and Au-based nanohole arrays with Ag nanoparticle decoration. *Chin. J. Phys.* **2026**, *100*, 1–9. [CrossRef]
10. Tang, X.; Hao, Q.; Hou, X.Y.; Lan, L.L.; Li, M.Z.; Yao, L.; Zhao, X.; Ni, Z.H.; Fan, X.C.; Qiu, T. Exploring and engineering 2D transition metal dichalcogenides toward ultimate SERS performance. *Adv. Mater.* **2024**, *36*, 2312348. [CrossRef] [PubMed]
11. Lan, L.L.; Gao, Y.M.; Fan, X.C.; Li, M.Z.; Hao, Q.; Qiu, T. The origin of ultrasensitive SERS sensing beyond plasmonics. *Front. Phys.* **2021**, *16*, 43300. [CrossRef]
12. Cao, Y.; Cheng, Y.; Sun, M. Graphene-based SERS for sensor and catalysis. *Appl. Spectrosc. Rev.* **2023**, *58*, 1–38. [CrossRef]
13. Ghosal, S.; Nandi, S.; Giri, P.K. Recent advances in semiconductor nanostructure-based surface-enhanced Raman scattering sensors. *Nanotechnology* **2025**, *36*, 202002. [CrossRef] [PubMed]
14. Ying, Y.; Fang, M.N.; Wang, C.Y.; Yan, Z.; Xie, H.; Wu, W.X.; Tang, Z.Y.; Liu, Y.L. Large-area ultrathin covalent-organic framework membranes for surface-enhanced Raman scattering: Optimal performance through thickness control. *Small* **2025**, *21*, 2501846. [CrossRef] [PubMed]
15. Figueiredo, J.S.; Fateixa, S.; Gouveia, J.D.; Gomes, J.R.B.; Trindade, T. Insights on charge-transfer mechanisms in ZnO and ZnO-GO substrates for the SERS analysis of 4-mercaptopyridine. *J. Phys. Chem. C* **2026**, *130*, 10618–10630. [CrossRef]
16. Tang, X.; Fan, X.C.; Zhou, J.; Wang, S.; Li, M.Z.; Hou, X.Y.; Jiang, K.W.; Ni, Z.H.; Zhao, B.; Hao, Q.; et al. Alloy engineering allows on-demand design of ultrasensitive monolayer semiconductor SERS substrates. *Nano Lett.* **2023**, *23*, 7037–7045. [CrossRef] [PubMed]
17. Fan, X.C.; Wang, R.; Li, M.Z.; Tang, X.; Xu, C.X.; Hao, Q.; Qiu, T. High-specificity molecular sensing on an individual whispering-gallery-mode cavity: Coupling-enhanced Raman scattering by photoinduced charge transfer and cavity effects. *Nanoscale Horiz.* **2023**, *8*, 195–201. [CrossRef] [PubMed]
18. Ge, Y.C.; Wang, H.Y.; Li, Q.H.; Li, Q.; Yang, Y.; Zhu, R.H.; Yang, J.M.; Liu, X.H.; Zhang, Q.W.; Wang, Y. Rapid and scalable preparation of highly uniform, atomically thin MSe_2 (M = Ti, Nb, Ta) nanosheets as ultra-sensitive SERS substrates for lateral flow immunoassay. *Adv. Funct. Mater.* **2025**, *35*, 2420786. [CrossRef]
19. Li, Y.H.; Bai, H.; Zhai, J.F.; Yi, W.C.; Li, J.F.; Yang, H.F.; Xi, G.C. Alternative to noble metal substrates: Metallic and plasmonic Ti_3O_5 hierarchical microspheres for surface enhanced Raman spectroscopy. *Anal. Chem.* **2019**, *91*, 4496–4503. [CrossRef] [PubMed]
20. Meng, X.Y.; Yu, J.; Shi, W.X.; Qiu, L.; Qiu, K.L.; Li, A.R.; Liu, Z.; Wang, Y.N.; Wu, J.J.; Lin, J.; et al. SERS detection of trace carcinogenic aromatic amines based on amorphous MoO_3 monolayers. *Angew. Chem. Int. Ed.* **2024**, *63*, e202407597. [CrossRef] [PubMed]
21. Patil, M.K.; Wagh, P.G.; Mukherjee, S.P. One-step microwave-assisted synthesis of a MoO_{3-x}-covalent organic framework (COF)-based nanocomposite for amplified surface-enhanced Raman spectroscopy in environmental applications. *Nanoscale* **2026**, *18*, 1345–1356. [CrossRef] [PubMed]
22. Gao, R.H.; Chen, L.; Li, Y.F.; Wang, Y.X.; Yang, T.Y.; Li, X.; Geng, J.; Guo, Z. Polyoxometalate cluster-guided dynamic nucleation and hierarchical growth of branched WO_3 nanofibers with ultrafine Pt nanoparticles for advanced gas sensing. *Inorg. Chem.* **2024**, *63*, 18285–18295. [CrossRef] [PubMed]
23. Garcia-Sanchez, R.F.; Ahmido, T.; Casimir, D.; Baliga, S.; Misra, P. Thermal effects associated with the Raman spectroscopy of WO_3 gas-sensor materials. *J. Phys. Chem. A* **2013**, *117*, 13825–13831. [CrossRef] [PubMed]
24. Xie, F.Y.; Gong, L.; Liu, X.; Tao, Y.T.; Zhang, W.H.; Chen, S.H.; Meng, H.; Chen, J. XPS studies on surface reduction of tungsten oxide nanowire film by Ar^+ bombardment. *J. Electron. Spectrosc.* **2012**, *185*, 112–118. [CrossRef]
25. Fan, X.C.; Li, M.Z.; Hao, Q.; Zhu, M.S.; Hou, X.Y.; Huang, H.; Ma, L.B.; Schmidt, O.G.; Qiu, T. High SERS sensitivity enabled by synergistically enhanced photoinduced charge transfer in amorphous nonstoichiometric semiconducting films. *Adv. Mater. Interfaces* **2019**, *6*, 1901133. [CrossRef]

26. Wang, F.; Di Valentin, C.; Pacchioni, G. Semiconductor-to-metal transition in WO_{3-x}: Nature of the oxygen vacancy. *Phys. Rev. B* **2011**, *84*, 073103. [CrossRef]
27. Colusso, A.V.; McDonagh, A.; Cortie, M.B. X-ray-induced reduction of a surfactant/polyoxotungstate hybrid compound. *Surf. Interface Anal.* **2025**, *50*, 1384–1388.
28. Tang, H.B.; Tang, Z.H.; Bright, J.; Liu, B.T.; Wang, X.J.; Meng, G.W.; Wu, N.Q. Visible-light localized surface plasmon resonance of WO_{3-x} nanosheets and its photocatalysis driven by plasmonic hot carriers. *ACS Sustain. Chem. Eng.* **2021**, *9*, 1500–1506. [CrossRef]
29. Guo, H.; Zhu, S.S.; Zhang, Z.H.; Pan, L.; Jiang, H.M.; Siddiqui, N.A.; Khan, A.; Lin, J.J. Oxygen vacancies and phosphorus-doped P-WO_{3-x}/CC electrocatalysts boosting hydrogen evolution reaction. *Chem. Eur. J.* **2025**, *31*, e202501239. [CrossRef] [PubMed]
30. Wattana, J.; Kansaard, T.; Mekprasart, W.; Boonyarattanakalin, K.; Pecharapa, W. Synthetic temperature-dependent photochromic properties of $W_{18}O_{49}$ materials synthesized by solvothermal method. *Radiat. Phys. Chem.* **2027**, *250*, 114296. [CrossRef]
31. Xu, J.; Li, Y.Y.; Wang, L.; Cai, Q.F.; Li, Q.W.; Gao, B.; Zhang, X.M.; Huo, K.F.; Chu, P.K. High-energy lithium-ion hybrid supercapacitors composed of hierarchical urchin-like WO_3/C anodes and MOF-derived polyhedral hollow carbon cathodes. *Nanoscale* **2016**, *8*, 16761. [CrossRef] [PubMed]
32. Zhang, L.; Wang, H.; Liu, J.B.; Zhang, Q.Q.; Yan, H. Nonstoichiometric tungsten oxide: Structure, synthesis, and applications. *J. Mater. Sci. Mater. Electron.* **2020**, *31*, 861–873. [CrossRef]
33. Li, M.; Wei, Y.; Fan, X.; Li, G.; Hao, Q.; Qiu, T. Mixed-dimensional van der Waals heterojunction-enhanced Raman scattering. *Nano Res.* **2022**, *15*, 637–643. [CrossRef]
34. Ketkong, A.; Thamaphat, K.; Sutthibutpong, T.; Nuntawong, N.; Chutrakulwong, F. TSNP-ink on PDMS: A flexible SERS substrate for damage-free agricultural pesticide detection. *Chemosensors* **2026**, *14*, 72. [CrossRef]
35. Phuc, L.G.; Do, P.Q.T.; Ta, H.K.T.; Dang, V.Q.; Joo, S.W.; Manh, D.; Bach, T.N.; Van, T.T.T.; Tran, N.H.T. Metal-enhanced fluorescence for alpha-fetoprotein detection and for SERS using hybrid nanoparticles of magnetic cluster core-plasmonic shell composite. *Chemosensors* **2023**, *11*, 56. [CrossRef]
36. Xie, T.; Li, P.; Wang, J.Z.; Dong, R.L.; Yang, L.B. Three-phase catassembly of 10 nm Au nanoparticles for sensitive and stable surface-enhanced Raman scattering detection. *Anal. Chem.* **2023**, *95*, 15293–15301. [CrossRef] [PubMed]
37. Shao, H.Z.; Wu, S.S.; Zhang, L.L.; Ye, B.H.; Luo, Q.Y.; Tong, K.Z.; Song, L.P.; Huang, Y.J. Skin-conformal sandwich-structured SERS superlattice platform for non-invasive depression detection. *ACS Sens.* **2026**, *11*, 2763–2773. [CrossRef] [PubMed]
38. Zhang, Y.; Huang, Y.; Zhai, F.; Du, R.; Liu, Y.; Lai, K. Analyses of enrofloxacin, furazolidone and malachite green in fish products with surface-enhanced Raman spectroscopy. *Food Chem.* **2012**, *135*, 845–850. [CrossRef] [PubMed]
39. Agrawal, A.; Cho, S.H.; Zandi, O.; Ghosh, S.; Johns, R.W.; Milliron, D.J. Localized surface plasmon resonance in semiconductor nanocrystals. *Chem. Rev.* **2018**, *118*, 3121–3207. [CrossRef] [PubMed]
40. Lan, L.L.; Hou, X.Y.; Gao, Y.M.; Fan, X.C.; Qiu, T. Inkjet-printed paper-based semiconducting substrates for surface-enhanced Raman spectroscopy. *Nanotechnology* **2020**, *31*, 055502. [CrossRef] [PubMed]
41. Chen, J.J.; Li, M.Y.; Wang, X.M.; Liu, H.Y.; Jiang, W.J.; Zhao, B.; Song, W. Putting charge transfer degree as a bridge connecting surface-enhanced Raman spectroscopy and photocatalysis. *Angew. Chem. Int. Ed.* **2025**, *64*, e202424986. [CrossRef] [PubMed]
42. Lan, L.L.; Zhao, C.Y.; Tang, X.; Gao, J.; Li, G.Q.; Cai, H.Y.; Yang, S.; Liu, J.; Qu, Z.W.; Fan, X.C.; et al. Charge-transfer-driven ultrasensitive SERS sensing in a two-dimensional titanium carbonitride MXene. *Opt. Lett.* **2024**, *49*, 2405–2408. [CrossRef] [PubMed]
43. Cong, S.; Yuan, Y.Y.; Chen, Z.G.; Hou, J.Y.; Yang, M.; Su, Y.L.; Zhang, Y.Y.; Li, L.; Li, Q.W.; Geng, F.X. Noble metal-comparable SERS enhancement from semiconducting metal oxides by making oxygen vacancies. *Nat. Commun.* **2015**, *6*, 7800. [CrossRef] [PubMed]
44. Zhang, L.; Yi, W.; Li, J.; Wei, G.; Xi, G.; Mao, L. Surfactant-free interfacial growth of graphdiyne hollow microspheres and the mechanistic origin of their SERS activity. *Nat. Commun.* **2023**, *14*, 6318. [CrossRef] [PubMed]
45. Xiao, Y.F.; Lan, L.L.; Ni, Z.H.; Tang, X.; Li, G.Q.; Zhao, X.; Hao, Q.; Fan, X.C.; Qiu, T. MXene-based micromotors: Active molecular enrichment and selective Raman enhancement. *J. Phys. Chem. Lett.* **2024**, *15*, 12535–12542. [CrossRef] [PubMed]

Disclaimer/Publisher's Note: The statements, opinions and data contained in all publications are solely those of the individual author(s) and contributor(s) and not of MDPI and/or the editor(s). MDPI and/or the editor(s) disclaim responsibility for any injury to people or property resulting from any ideas, methods, instructions or products referred to in the content.